Selective laser melting additive manufacturing of TiC/Inconel 718 bulk-form nanocomposites: Densification, microstructure, and performance

Qingbo Jia
College of Materials Science and Technology, Nanjing University of Aeronautics and Astronautics, 210016 Nanjing, People's Republic of China; and Institute of Additive Manufacturing (3D Printing), Nanjing University of Aeronautics and Astronautics, 210016 Nanjing, People's Republic of China

Dongdong Gu[a)]
College of Materials Science and Technology, Nanjing University of Aeronautics and Astronautics, 210016 Nanjing, People's Republic of China; and Institute of Additive Manufacturing (3D Printing), Nanjing University of Aeronautics and Astronautics, 210016 Nanjing, People's Republic of China

(Received 2 April 2014; accepted 2 June 2014)

Selective laser melting (SLM) process was used to prepare the nanocrystalline titanium carbide (TiC)-reinforced Inconel 718 matrix bulk-form nanocomposites in the present study. An in-depth relationship between SLM process, microstructures, properties, and metallurgical mechanisms was established. The insufficient laser energy density (η) input limited the densification response of shaped parts due to the formation of either larger-sized pore chains or interlayer micropores. The densification of SLM-processed part increased to a near-full level as the applied η was properly settled. The TiC reinforcements generally experienced successive changes from severely agglomerated in a polygon shape to the uniformly distributed with smoothened and refined structures on increasing the applied η, while the columnar dendrite matrix exhibited strong epitaxial growth characteristic concurrently. The optimally prepared fully dense part achieved a high microhardness with a mean value of 419 $HV_{0.2}$, a considerably low friction coefficient of 0.29, and attendant reduced wear rate of 2.69×10^{-4} mm^3/N m in dry sliding wear tests. The improved densification response, SLM-inherent nonequilibrium metallurgical mechanisms with resultant uniformly dispersed reinforcement microstructures, and elevated microhardness were believed to be responsible for the enhancement of wear performance.

I. INTRODUCTION

Nickel-based superalloys are typically used as high-temperature service parts in industrial and aerospace fields where good combination of high workability and mechanical properties are required.[1] Inconel 718, a Ni–Cr–Fe-based austenitic superalloy, has found wide applications including in gas turbine wheel blades, nuclear reactors, containers, and fossil fuel components, due to its outstanding creep performance, tensile properties, oxidation resistance, and hot corrosion resistance.[2] As the most attractive candidate material of hot-end components, Inconel 718 can retain its mechanical strength over a wide range of temperatures. This high-temperature strength was confirmed to be attributable to the inherent solid-solution strengthening and/or precipitation strengthening mechanisms.[3] Though the Inconel 718 alloy was originally developed for the manufacture of gas turbine wheel blades four decades ago, it has found extensive applications in various fields afterward and still been regarded as today's most widely used superalloy in the world.[4] Particularly, the environments that Inconel 718 superalloy has been subjected in the above applications generally involved a wide variety of corrosion, oxidation, and wear at elevated temperatures. Nevertheless, with the rapid development of modern industry, still higher-performing Inconel 718 parts are on increasing demand as working conditions of hot-end components reached ever higher temperatures in search of greater efficiency.

Metal matrix composites (MMCs), reinforced with discontinuous ceramic reinforcements, are considered as important structural materials, owing to their high specific modulus and strength, high stiffness, and good fatigue properties.[5,6] Unlike the continuous fiber reinforcements, the incorporation of ceramics in a raw powder material form to obtain discontinuously reinforced MMCs is widely believed to be one of the most cost-effective and environmentally protective strategies.[7] The MMCs demonstrate their superiority compared with the pure parts for significantly increased not only of high harness (wear resistance), but also of high-temperature mechanical performance.[8] Nevertheless, the interfacial bonding ability between the hard reinforcements and the relatively ductile

a)Address all correspondence to this author.
e-mail: dongdonggu@nuaa.edu.cn
DOI: 10.1557/jmr.2014.130

 © Materials Research Society 2014

https://doi.org/10.1557/jmr.2014.130 Published online by Cambridge University Press

metal matrix, which govern the overall mechanical properties of MMCs, is generally limited due to the poor wettability between the ceramic particles and metals. The weak bonding presented at the ceramic/metal interface is prone to crack during the mechanical loading, leading to the premature failure of MMCs (reinforced with discontinuous ceramic reinforcements). Generally, this problem may become even aggravated as larger-sized particles are incorporated to form the MMCs.

It is well known that the particle size played a key role in determining the strength, ductility, and the failure mode of MMCs. Higher surface-to-volume ratio of reinforcements can be obtained on decreasing the ceramic particle size, which may bring about the significant improvement of interfacial adhesion performance.[9] Based on this point of view, recent research attempts have focused on studies of nanocomposites by decreasing the reinforcement particle size down to nanometer level.[10] To achieve substantial increment of mechanical properties of nanocomposites, the densification response should be ascertained by the process technique as the same is of primary importance. On the other hand, the technical challenge of agglomeration behavior that occurred between the nanopowders due to the large van der Waals attractive force should also be taken into consideration, for obtaining homogeneous microstructures and the resultant enhanced mechanical properties.

Selective laser melting (SLM), as a laser-based material additive manufacturing (AM) technology, has the unique capability of quick production of three-dimensional (3D) objects with an almost unchallenged freedom of design.[11] During the SLM shaping process, the computer-aided design (CAD) model of the user-designed component is sliced into layers mathematically and the attendant layer files are transmitted to a computer-controlled manufacturing system. The component is then built using a high-energy laser beam to fuse and consolidate the prespread loose powders selectively according to the corresponding two-dimensional (2D) cross-section of the sliced object CAD model in a layer-by-layer way. SLM is processed based on a full melting/solidification mechanism involving a unique nonequilibrium nature, wherein the laser irradiated zone can rapidly heated up to 10^5 K and followed by a rapid cooling at a rate up to 10^{6-7} K.[12] It thus provides the high potential for development of nonequilibrium phases with fine-grained microstructures and novel metallurgical properties.[12] As per recent developments, the application of SLM technology is expected to produce nanocomposites with sound mechanical property performance. Nevertheless, significant research efforts are still required to study the metallurgical mechanism and microstructural development due to the complicated physical nature of SLM, in which multiple modes of heat, mass, and momentum transfer induced by a dynamic laser scanning were involved.[13]

In the present investigation, SLM was applied to prepare the TiC/Inconel 718 nanocomposites in bulk-form. The microstructural characteristics at various laser processing conditions were studied and the mechanical performance in terms of densification, microhardness, and wear resistance was assessed. The objective of this work is to establish a relationship between processing conditions, microstructural characteristics, and mechanical performance of TiC/Inconel 718 nanocomposites and provide a corresponding theoretical basis which may applicable and/or transferable to other laser-based techniques.

II. EXPERIMENTAL PROCEDURES

A. Powder preparation

The gas-atomized, spherical Inconel 718 powder with a size distribution of 15–45 μm and the polygonal-shaped TiC nanopowder in an average particle size of 50 nm were used as starting materials in this study. The chemical compositions of Inconel 718 powder are 21.35 chromium (Cr), 20.47 iron (Fe), 1.15 Titanium (Ti), 0.8 aluminum (Al), 4.75 niobium (Nb), 2.8 molybdenum (Mo), 0.08 carbon (C), and balance nickel (Ni) (wt%). The Inconel 718 and TiC components in a weight ratio of 9:1 were homogeneously mixed in a Fritsch Pulverisette 6 planetary ball mill (Fritsch GmbH, Germany) using a ball-to-powder weight ratio of 5:1, a rotation speed of the main disc of 200 rpm, and a milling time of 4 h.

B. SLM process

The TiC/Inconel 718 parts were processed using a SLM experimental setup that mainly consisted of a continuous wave IPG Photonics Ytterbium YLR-200-SM (IPG Laser GmbH, Germany) fiber laser with a maximum output power of 200 W, an automatic powder delivery apparatus, an inert argon gas protection system, and a computer system for process control. The schematic of SLM process is plotted in Fig. 1(a). When specimens were to be prepared, all the SLM experiments were conducted in an argon environment with an outlet pressure of 30 mbar and the resultant oxygen concentration decreased below 10 ppm. Based on a series of preliminary experiments, the three main parameters involved in the shaping process including the constant laser scan speed (v) at 400 mm/min, the laser beam diameter (d) of 70 μm, and the laser power (P) varied from 80 to 130 W. An integrated parameter "laser energy density" (η), which was defined by:

$$\eta = \frac{4P}{v\pi d^2} \quad , \tag{1}$$

was used to estimate the laser energy input to the powder layer being processed. Thus four different laser energy densities η of 3, 3.9, 4.7, 5.1 kJ/mm^3 were determined to

https://doi.org/10.1557/jmr.2014.130 Published online by Cambridge University Press

study the influence of different laser parameters on processability and attendant microstructural and mechanical properties of SLM-processed composite parts. The bulk-form specimens with dimensions of 8 mm × 8 mm × 6 mm were successfully shaped in a layer-by-layer way. The as-prepared nanocomposite parts exhibited good surface finish and sample integrity without dimensional distortion [Fig. 1(b)].

C. Microstructural and mechanical properties characterization

Phase identifications of SLM-processed TiC/Inconel 718 composite parts were performed by a D8 Advance x-ray diffractometer with Cu K_α radiation at 40 kV and 40 mA, using a continuous scan mode. The fabricated samples were mounted, polished, and etched in line with the standard procedures for metallographic observation. Microstructures were characterized using a scanning electron microscopy (SEM; Hitachi model S-4800, Japan) at an accelerating voltage of 3 kV, fitted with an energy dispersive x-ray spectroscopy (EDX, EDAX Inc.) system.

The Vikers hardness was measured using a HXS-1000A microhardness tester (Shanghai Precision Instruments, China) at a load of 0.2 kg and an indentation time of 20 s. Dry sliding wear tests were carried out in a HT-500 ball-on-disk tribometer at room temperature. A 3-mm diameter bearing steel GCr15 ball with a mean hardness of HRC60 was taken as the counterface material, using a test load of 4.3 N. The friction unit was rotated at 560 rpm for 15 min and the rotation radius was 2 mm. The coefficient of friction (COF) was recorded during the sliding tests. The wear volumes (V) of specimens were determined gravimetrically using:

$$V = \frac{M_{\text{loss}}}{\rho} \quad , \tag{2}$$

where M_{loss} was the weight loss of specimens after tests and ρ was the density. The wear rates (ω) were calculated by:

$$\omega = \frac{V}{WL} \quad , \tag{3}$$

where W was the contact load and L was the sliding distance.

III. RESULTS AND DISCUSSION

A. Phase identification

The typical x-ray diffraction (XRD) patterns of SLM-processed TiC/Inconel 718 parts under various processing conditions are depicted in Fig. 2. Generally, the strong diffraction peaks belong to Ni–Cr–Fe matrix and the TiC

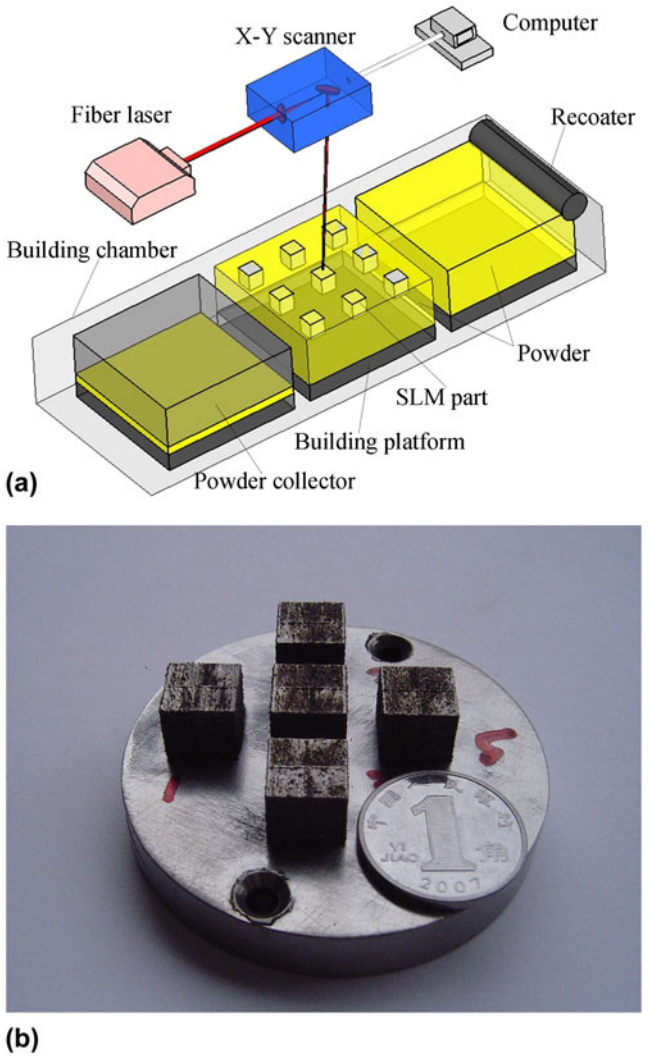


FIG. 1. (a) Schematic of SLM process and (b) photograph of processed parts.

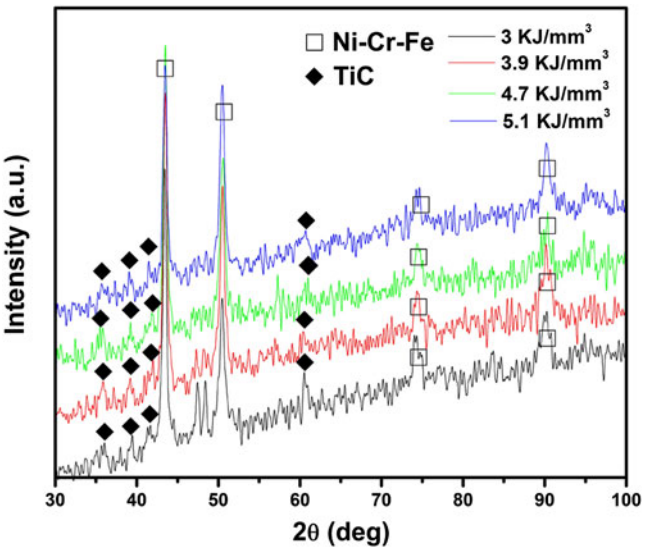


FIG. 2. XRD spectra of SLM-processed parts at different laser energy densities.

https://doi.org/10.1557/jmr.2014.130 Published online by Cambridge University Press

phase in weak peak intensities were detected. As viewed in Fig. 2, the 2θ locations of matrix phases in SLM-processed parts shifted to higher Bragg angles on increasing the input laser energy density, which was believed to be caused by the distortion of lattice due to the incorporation of TiC reinforcing particles throughout the matrix.[14] A careful comparison showed that the TiC diffraction peak became considerably broadened while the peak intensities decreased with the enhancement of the applied η, implying the formation of refined TiC grains of SLM-processed parts.

B. Densification behavior

Figure 3 shows the appearance of molten pool within the vertical sections of SLM-processed TiC/Inconel 718 parts. In experiments, the relative density of SLM-processed specimens was determined on the basis of Archimedes method in deionized water. The changes in measured relative densities of corresponding parts are illustrated in Fig. 4. The molten pool morphologies experienced significant changes with different laser energy density inputs. Layerwise microstructural features were generally observed as a result of the layer-by-layer deposition manner of the SLM shaping process. At a lower η of 3 kJ/mm^3, larger-sized pore chains which crossed over multiple layers were clearly observed [Fig. 3(a)]. The molten pool morphology in irregular and poorly bonded characteristics was observed between the neighboring scanning tracks and layers, leading the densification response by merely 80.7% (Fig. 4). On increasing the applied η by enhancing the input laser power, irregular micropores were found to be diminished and dispersed within the interlayer bonding areas even though the distribution state of layers were still uneven, resulting in a markedly increased densification rate of 92.4% [Figs. 3(b) and 4]. At an even higher η of 4.7 kJ/mm^3, only a few micropores were formed within the molten pool and the obtained densification rate in this instance approached 96.6% [Figs. 3(c) and 4]. As η of 5.1 kJ/mm^3 was properly settled, sound vertical-section morphology free of any pores with a near-full densification level of 98.3% was obtained [Figs. 3(d) and 4]. It should also be noted that the metallurgical bonding between the adjacent layers and scanning tracks was both well developed in the latter two cases.

During the SLM AM process, the molten pool in each layer was comprised of the previously solidified materials as well as the freshly deposited powder particles. This characteristic was particularly important for obtaining the stable bonding property between each layer, which also guaranteed the densification behavior and microstructural development of the whole part. In the present study, the success of obtaining dense and homogeneously distributed layers hinged on the coordination of the SLM conditions used during the shaping process. At an insufficient laser power input, weak interlayer bonding can occur due to the poor dilution between the previously solidified materials and the freshly spread layer, leaving the interlayer pores in the finished part. In this case, less energy was absorbed within the molten pool and the resultant temperature was

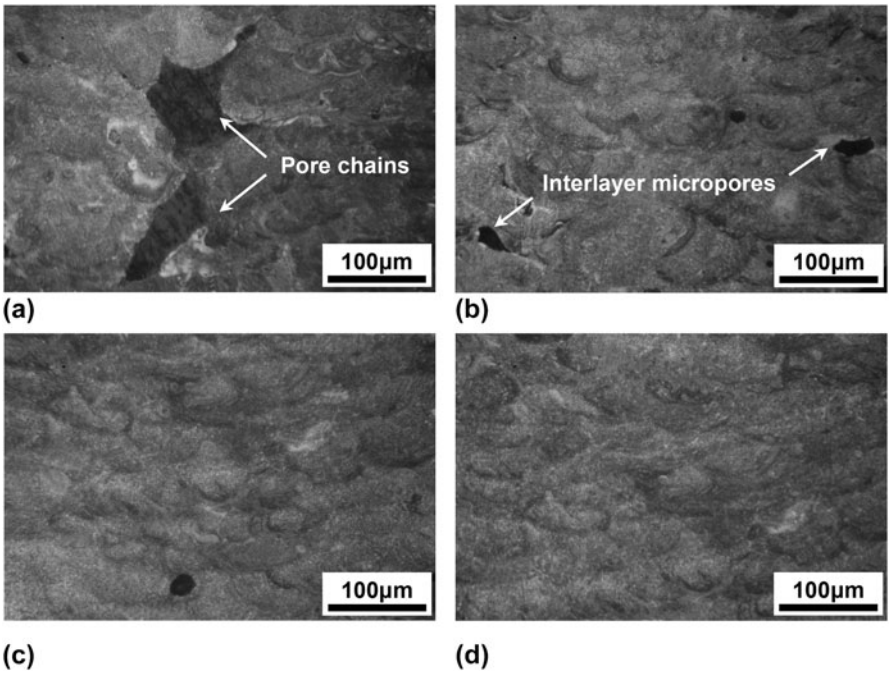


FIG. 3. Optical microscopy images showing interlayer microstructures of SLM-processed parts under different SLM conditions: (a) 3 kJ/mm^3; (b) 3.9 kJ/mm^3; (c) 4.7 kJ/mm^3; (d) 5.1 kJ/mm^3.

https://doi.org/10.1557/jmr.2014.130 Published online by Cambridge University Press

relatively low, which caused insufficient melting of the reinforcements. According to previous study,[15] the viscosity of a solid–liquid mixture (μ) is dependent on the operative temperature *(T)* within the molten pool and is inversely proportional to *T*. Thereby the dynamic viscosity was enhanced at a lower operative temperature and thus inhibited the melted liquid from spreading out smoothly, which in turn caused the formation of weak bonding between the neighboring scanning tracks and the resultant limited densification response. As the optimum laser parameters were preset, the densification rate can be markedly improved lying in the good bonding capability between the neighboring layers and scanning tracks.

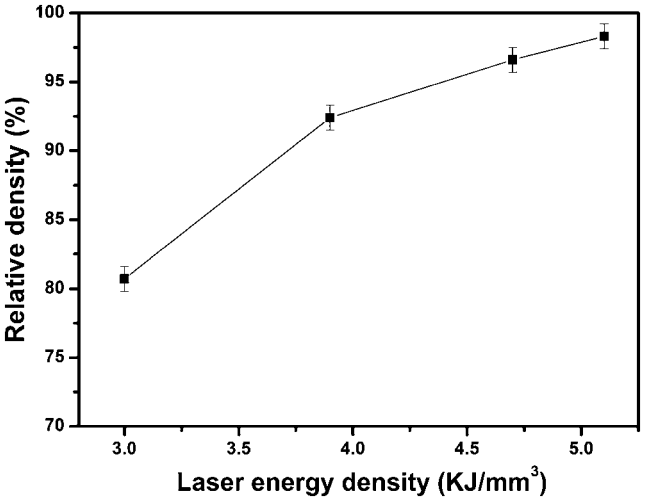


FIG. 4. Effect of laser energy density on densification response of SLM-processed parts.

Besides the above analyses, the wettability between the ceramic particles and the Inconel matrix also played a significant role in determining the densification behavior of SLM-processed composite parts. For a reactive wetting system of liquid metals on ceramic phase, the equilibrium contact angle θ_{eq} can be approximately assessed as:[16]

$$\cos\theta_{eq} = (\gamma_{sv} - \gamma_{ls})/\gamma_{lv} \quad , \tag{4}$$

where γ_{lv}, γ_{sv}, and γ_{ls} are the interface tensions of liquid metal-vapor, reacted ceramic-vapor, and liquid metal-reacted ceramic, respectively. γ_{lv} may vary during reaction as the reaction product may diffuse into the liquid while γ_{ls} was normally in linear negative correlation with the operating temperature.[17] An increment in the applied η elevated the worktable temperature and lowered γ_{ls}, which accordingly decreased the contact angle on basis of the above equation. The improved liquid wettability was therefore obtained, favoring sufficient consolidation and elevating the densification level of the SM-processed composite system.

C. Microstructural characteristics

Figure 5 shows the influence of applied η on microstructural evolutions of SLM-processed TiC/Inconel 718 composite parts at a relatively lower magnification. Higher magnifications on specific positions were used, as shown in Fig. 6, for studying the corresponding characteristic

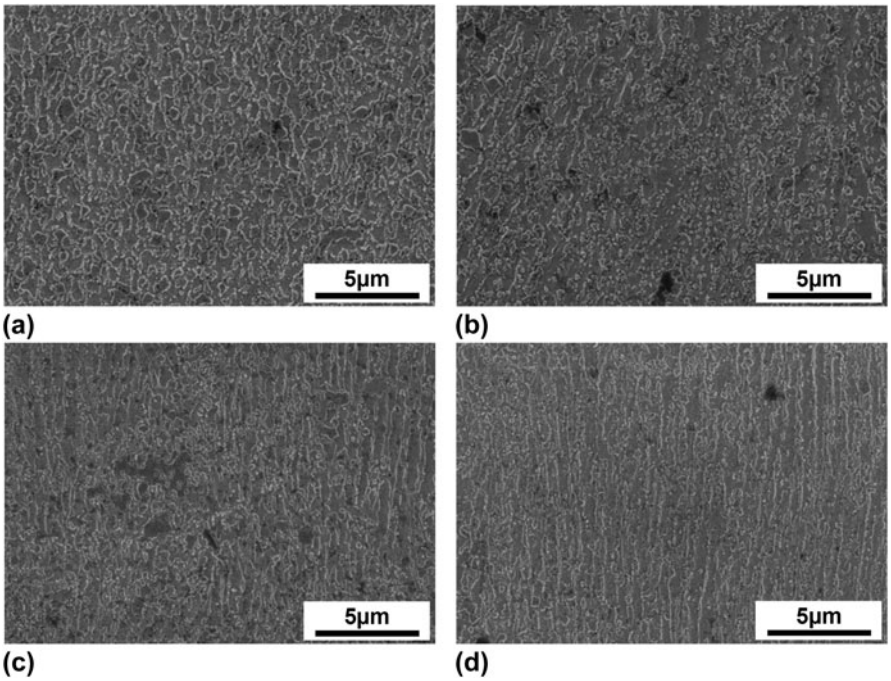


FIG. 5. SEM images showing typical microstructures on the etched vertical-sections of SLM-processed parts at different laser energy densities: (a) 3 kJ/mm^3; (b) 3.9 kJ/mm^3; (c) 4.7 kJ/mm^3; (d) 5.1 kJ/mm^3.

https://doi.org/10.1557/jmr.2014.130 Published online by Cambridge University Press

microstructures. At a lower input η of 3 kJ/mm^3, intermittent dendrites combined with crystalline lumps were observed [Fig. 5(a)]. The quantitative element analysis by EDX revealed that the lumps were mainly composed of Ni, Cr, and Fe elements, indicating that the lumps were part of the columnar dendrites. Higher magnifications revealed that the TiC reinforcements, which were proved by EDX analysis with an atomic ratio approximately to 1:1 of Ti and C elements, experienced severe agglomerations during the solidification process [Fig. 6(a)]. As the applied η increased to 3.9 kJ/mm^3, large amounts of particles could be observed, whereas the amounts of lumps decreased to a great extent [Fig. 5(b)]. The submicrometer-sized TiC reinforcements in an initial polygon structure could be distinguished even though the particles were still found to be agglomerated at a magnified state [Fig. 6(b)]. On increasing the applied η to 4.7 kJ/mm^3, a typical epitaxial growth of columnar dendrites was formed in this instance [Fig. 5(c)]. The surface of the TiC reinforcing particles became apparently smoothened and its dispersion state became much more homogeneous [Fig. 6(c)]. As the further enhanced η of 5.1 kJ/mm^3 was properly settled, the directionally solidified slender columnar dendrites were obtained [Fig. 5(d)]. The observed reinforcement particles became significantly refined, which was in good accordance with the XRD analyses, exhibited a near spherical morphology with an average size of ~50 nm and a uniformly dispersed state throughout the matrix [Fig. 6(d)]. It should be noted that the nanomaterials can be defined as materials which have structured components with size less than 100 nm in at least one dimension.[18] On this basis, it can be concluded that the SLM-processed TiC/Inconel 718 nanocomposite part with uniformly distributed nanostructured TiC reinforcements was obtained in this case. In this instance, ultrafine round particles were also clearly observed throughout the columnar matrix, which were believed to be precipitations obtained during the nonequilibrium solidification process in our previous study.[19]

In the process of SLM, the energy is rapidly absorbed by the powder materials through both bulk-coupling and powder-coupling mechanisms as the high-energy laser beam scans over the powder bed.[20] Basically, most of the heat induced by laser irradiation was dissipated through the substrate or previously solidified materials, leading to an important thermal temperature gradient along the building direction. This facilitated the nucleation and epitaxial growth of the typical columnar dendrite architectures toward the opposite heat transmitting direction, which have also been found by other authors working on AM processes of nickel-based superalloys.[21,22] The variations of internal energy and thermodynamic potentials caused by heat accumulation and temperature development under different laser energy densities were believed to be responsible for the microstructure changes.[23] According to previous study,[24] the high *G*/*R* (*G* is the temperature gradient and *R* is the solidification speed of crystals) was regarded as the driven force for the nucleation and growth of crystallographically oriented columnar dendrites. With the increment of the input laser energy density, the working temperature could be elevated

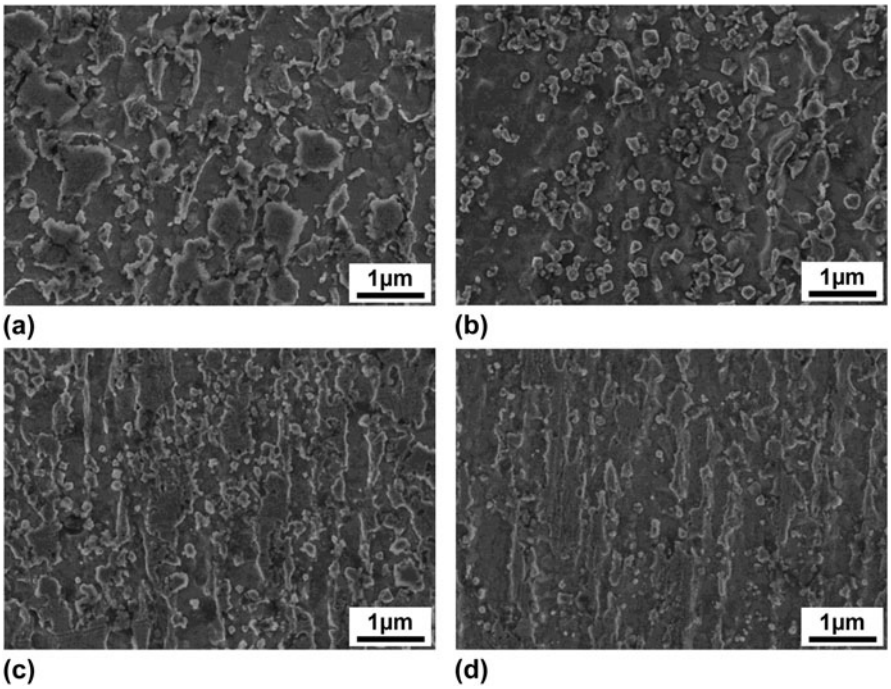


FIG. 6. High-magnification SEM-images showing characteristic microstructures in SLM-processed parts in (a) Fig. 5(a); (b) Fig. 5(b); (c) Fig. 5(c); (d) Fig. 5(d).

https://doi.org/10.1557/jmr.2014.130 Published online by Cambridge University Press

while the liquid cooling time became comparatively prolonged as more energies were absorbed within the molten pool. This provided the strengthened thermal kinetic conditions for the directional growth of columnar dendrites by improving the temperature gradient and the resultant decrement of crystal solidification speed.

As the applied laser energy density increased, more liquid contents were formed within the molten pool due to the elevated temperature and subsequently melted powders around. The edges of the reinforcements were therefore melted with sufficient wetting of the surrounding liquid in the molten pool, favoring significant smoothening and refinement of the initially added TiC particles. On the other hand, the distribution state of the reinforcement particles mainly depended on the interactions between the solid particles and the dynamic Marangoni flow within the micrometer-sized molten pool.[25] During the SLM shaping process, the laser beam power in a Gauss energy distribution was taken as the energy source to melt the prespread composite powders. The surface tension gradient within the molten pool would necessarily be generated as a result of the local temperature gradient and chemical concentration gradient, leading to the formation of Marangoni convection. The liquid capillary force was therefore formed under the function of the convective stream within the molten pool, which subsequently exerted on the solid particles and facilitated its movement and rearrangement. However, it is worth noting that the intensity of the Marangoni flow was inversely proportional to the viscosity within the molten pool.[26] As elucidated previously, the viscosity of the present solid/liquid composite system is dependent on the working temperature and changes inversely with it. Therefore, as the applied laser energy density increased, the intensified Marangoni flow resulting from the reduced viscosity can effectively accelerate the rearrangement of solid particles, favoring the formation of TiC/Inconel 718 nanocomposites with uniformly distributed reinforcements.

D. Microhardness and wear performance

The average microhardness values measured on the polished sections of SLM-processed TiC/Inconel 718 composite parts are depicted in Fig. 7. On increasing the applied η from 3 kJ/mm^3 to 5.1 kJ/mm^3, the microhardness increased markedly from 360 $HV_{0.2}$ to 419 $HV_{0.2}$. It should be pointed out that the mean microhardness has exceeded that of the ordinary smelted pure Inconel 718 parts followed by heat treatment (383 $HV_{0.2}$) as applied η increased to 3.9 kJ/mm^3 (386 $HV_{0.2}$). Obviously, the improved densification behavior and uniformly distributed microstructures were the main contributions for the microhardness enhancement of SLM-processed composite parts. Moreover, the matrix grains of SLM-processed parts were normally much finer than those obtained by conventional casting procedures or other laser processing technologies based on powder blow feeding, due to the micrometer-sized molten pool induced by the focalized laser spot and the elaborately prespread powder layers with thickness of merely dozens of micrometer. This undoubtedly made considerable contributions to the improvement of microhardness of SLM-processed parts by virtue of the fine grain strengthening effect. Nevertheless, the effect of precipitations also played a significant role on microhardness improvement by virtue of its inherent higher hardness as well as the distinctive lattice structure compared with the columnar matrix.

The changes of friction coefficients and wear rates of SLM-processed composite parts are illustrated in Figs. 8 and 9, respectively. Compared with our previous study,[19] the incorporation of TiC reinforcements into the Inconel 718 matrix indeed showed quite good wear resistance as relative to the pure Inconel 718 parts under the same SLM condition. In general, the COF curves all exhibited severe fluctuation at the initial running-in stage of the wear test.

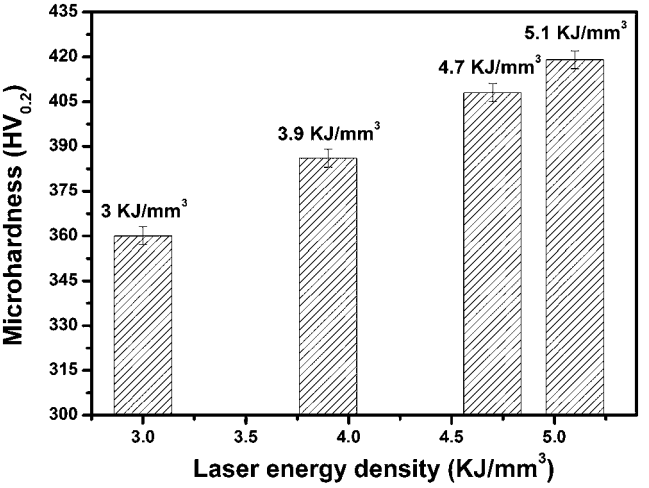


FIG. 7. Microhardness of SLM-processed parts under various SLM processing conditions.

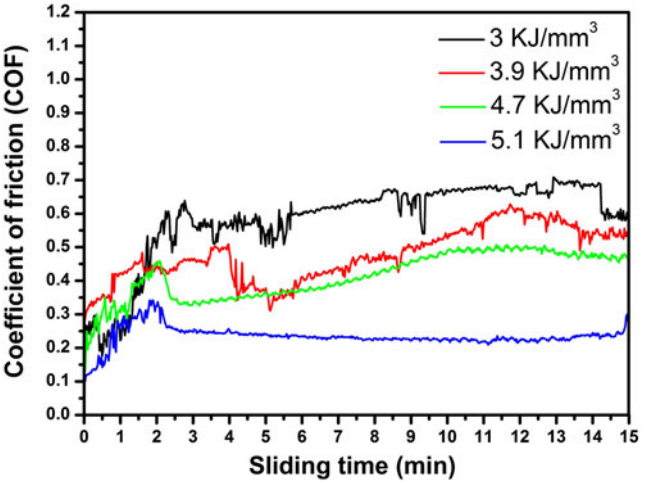


FIG. 8. Effect of laser energy densities on COFs of SLM-processed parts.

https://doi.org/10.1557/jmr.2014.130 Published online by Cambridge University Press

This was attributed to the relatively higher surface roughness that led to the reduced contact area between wear counterparts and the resultant severe fluctuation of the COF. With the sliding friction process extending, the fluctuation behavior of the COF became leveled off owing to the decreased surface roughness.

The COF fluctuations reduced significantly with the increment of the input laser energy density in the present study. At a relatively low η of 3 and 3.9 kJ/mm^3, the COFs with respective average values of 0.58 and 0.46 both showed severe fluctuations with sliding time extension. In these two cases, the wear rates were accordingly measured to be 5.7×10^{-4} and 4.44×10^{-4} mm^3/N m. This fluctuation behavior became alleviated and the average COF value decreased to 0.41 at a higher η of 4.7 kJ/mm^3, resulting in a reduced wear rate of 3.71×10^{-4} mm^3/N m. As the proper η was settled at 5.1 kJ/mm^3, an average COF value of 0.29 was obtained, in which the wear rate decreased to the lowest of 2.69×10^{-4} mm^3/N m.

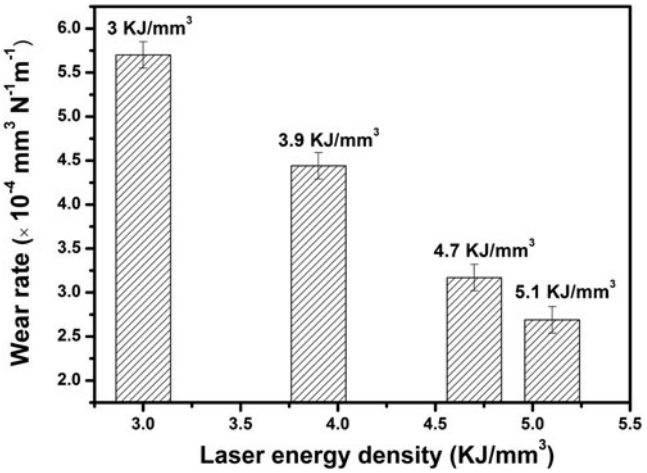


FIG. 9. Wear rates of SLM-processed parts using different processing parameters.

Figure 10 illustrates the detailed SEM photograph investigations on the corresponding worn surfaces of the SLM-processed composite parts. Higher magnifications on specific locations in structures were also studied, as shown in Fig. 11, for having a better understanding of the inherent wear mechanisms. As is clear in the images, the worn surface morphologies varied greatly from the applied laser energy density and the wear mechanism in the present study was primarily dominated by adhesive and abrasive types of wear. At a lower η of 3 kJ/mm^3, the surface roughness of the worn parts was relatively high with evidence of observed severe material delamination and spallation [Fig. 10(a)], leading to higher material loss and COF fluctuation behavior. Higher magnifications revealed that the flake-like wear scars were found to be adherent on the worn surface which were believed to be the typical characteristics of adhesive wear [Fig. 11(a)]. Mild scratches with less wear debris residual were formed on the worn surface as η increased to 3.9 kJ/mm^3 [Fig. 10(b)]. Closer investigation revealed that the wear debris was mainly composed of ultrafine grains, which contributed to the severe COF fluctuations in this case [Fig. 11(b)]. The worn surface

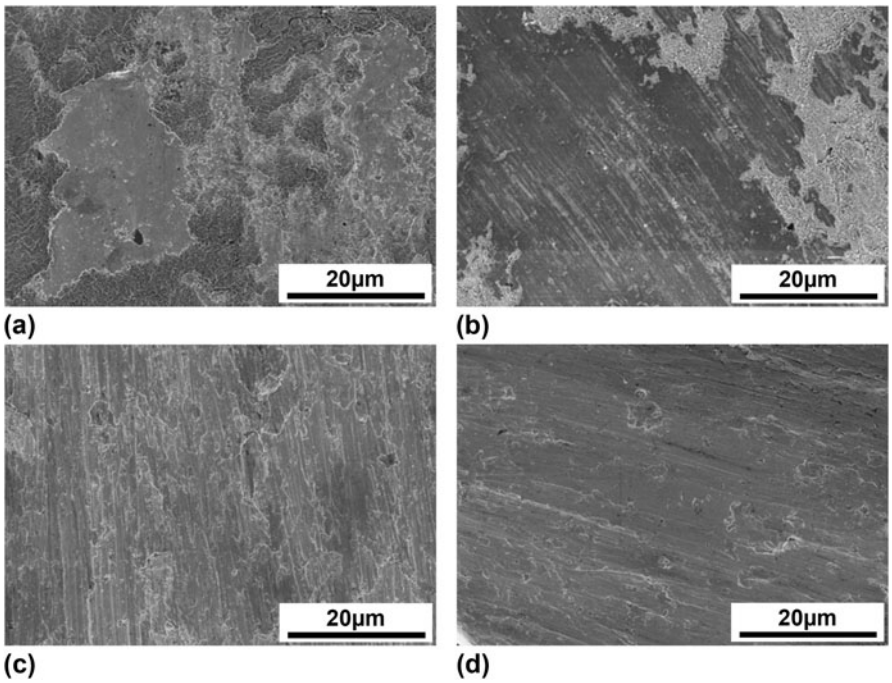


FIG. 10. SEM images showing worn surface morphologies on SLM-processed parts under various laser energy densities: (a) 3 kJ/mm^3; (b) 3.9 kJ/mm^3; (c) 4.7 kJ/mm^3; (d) 5.1 kJ/mm^3.

https://doi.org/10.1557/jmr.2014.130 Published online by Cambridge University Press

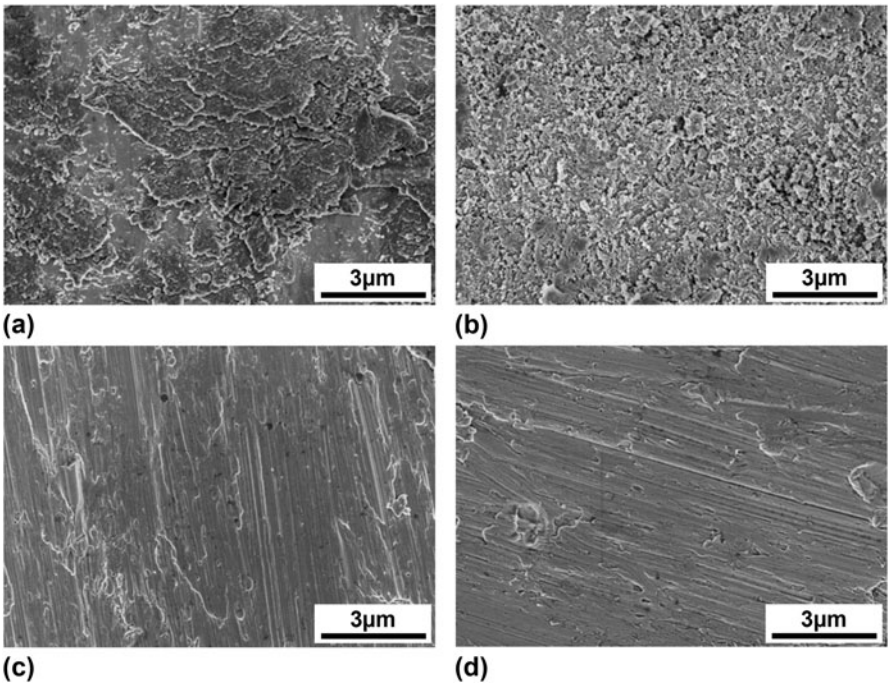


FIG. 11. High-magnification SEM images showing characteristic worn surface morphologies in SLM-processed parts in (a) Fig. 10(a); (b) Fig. 10(b); (c) Fig. 10(c); (d) Fig. 10(d).

became much smoother and free of any wear fragments on increasing the applied η to 4.7 kJ/mm^3, whereas shallow grooves and slight plastic deformation were still obtained at a magnified state [Figs. 10(c) and 11(c)]. In this instance, it was pertinent to conclude that the dominant mechanism changed to being largely abrasion wear. On increasing the applied η to 5.1 kJ/mm^3, smooth and dense wear tracks were obtained eventually, showing no apparent fractures on the worn surface [Figs. 10(d) and 11(d)].

During the present study, the dry sliding wear tests were measured based on the interaction between the counterface ball and the subjected parts, wherein the densification level, microstructures, and microhardness exerted a basic role in determining the wear properties. At a lower laser energy density input, the limited relative density and microhardness were believed to be responsible for the higher wear rate due to the shearing force acting between the sliding surfaces. Massive materials were pulled out under the effect of the friction force and the penetration inside the sample, causing the wear mechanism to change from two-body to three-body wear mechanism. As the sliding action continued, the loss debris became work hardened and then welded themselves to the surface of the wear track driven by the friction generated heat, which in turn resulted in highly fluctuating friction coefficients as a result of the moving parts sticking.[27] On increasing the applied laser energy density, the densification level and microhardness of fabricated parts were comparatively improved. The loose wear debris was crushed into ultrafine grains under the roller compaction effect between the friction pairs, resulting in exacerbated fluctuations of COFs. The wear resistance can be markedly enhanced on increasing the applied laser energy density by virtue of the obtained even-higher densification level and microhardness.[28] This directly resulted from the significantly improved load capability and the resultant decreased contact area of the subjected samples. Moreover, the uniformity of the reinforcement microstructures also exerted an important role in influencing the stability of friction coefficients. The uniformly distributed hard reinforcements in the composite material could act as a supporting net, which provided excellent wear resistance albeit against the abrasion of the counterface ball and wear debris.

IV. CONCLUSIONS

(i) The densification activity of SLM-processed TiC/Inconel 718 parts was controlled by the applied laser energy density. A near-full 98.3% density was obtained as a laser energy density of 5.1 kJ/mm^3 was properly settled, while the samples prepared at other SLM conditions showed different degrees of decrement due to the formations of either larger-sized pore chains or interlayer micropores.

(ii) The TiC reinforcements experienced successive changes on increasing the applied laser energy density: severely agglomerated – polygon structured – smoothened and refined, while the distribution state of which became more and more homogeneous. The epitaxial growth characteristic of the columnar dendrite matrix was markedly enhanced with the increment of laser energy density.

https://doi.org/10.1557/jmr.2014.130 Published online by Cambridge University Press

(iii) As the applied laser energy density was properly settled, the prepared TiC/Inconel 718 nanocomposite part possessed higher microhardness with a mean value of 419 $HV_{0.2}$. A uniform distribution of friction coefficient with a considerably lower average value of 0.29 and a reduced wear rate of 2.69×10^{-4} mm^3/N m was obtained during the dry sliding wear tests, which can be attributed to the improved densification level, microhardness, and the uniformly dispersed reinforcement microstructures.

ACKNOWLEDGMENTS

The authors gratefully appreciate the financial support from the National Natural Science Foundation of China (No. 51322509 and No. 51104090), the Outstanding Youth Foundation of Jiangsu Province of China (No. BK20130035), the Program for New Century Excellent Talents in University (No. NCET-13-0854), the Program for Distinguished Talents of Six Domains in Jiangsu Province of China (No. 2013-XCL-028), the Fundamental Research Funds for the Central Universities (No. NE2013103), and the Qing Lan Project, Jiangsu Provincial Department of Education, China. Qingbo Jia appreciates the support from the Foundation of Graduate Innovation Center in Nanjing University of Aeronautics and Astronautics (No.kfjj20130218).

REFERENCES

1. K.N. Amato, S.M. Gaytan, L.E. Murr, E. Martinez, P.W. Shindo, J. Hernandez, S. Collins, and F. Medina: Microstructures and mechanical behavior of Inconel 718 fabricated by selective laser melting. *Acta Mater.* **60**, 2229 (2012).
2. G. Cam and M. Kocak: Progress in joining of advanced materials. *Int. Mater. Rev.* **43**, 1 (1998).
3. C. Slama, C. Servant, and G. Cizeron: Aging of the Inconel 718 alloy between 500 and 750°C. *J. Mater. Res.* **12**, 2298 (1997).
4. M.S. Seehra and V.S. Babu: Low temperature magnetic transition and high temperature oxidation in Inconel alloy 718. *J. Mater. Res.* **11**, 1133 (1996).
5. I.A. Ibrahim, F.A. Mohamed, and E.J. Lavernia: Particulate reinforced metal matrix composite – A review. *J. Mater. Sci.* **26**, 1137 (1991).
6. X.L. Wu: Microstructural characteristics of TiC-reinforced composite coating produced by laser syntheses. *J. Mater. Res.* **14**, 2704 (1999).
7. D.D. Gu and Y.F. Shen: Microstructures and properties of direct laser sintered tungsten carbide (WC) particle reinforced Cu matrix composites with RE-Si-Fe addition: A comparative study. *J. Mater. Res.* **24**, 3397 (2009).
8. D.D. Gu, W. Meiners, K. Wissenbach, and R. Poprawe: Laser additive manufacturing of metallic components: Materials, processes, and mechanisms. *Int. Mater. Rev.* **57**, 133 (2012).
9. S.C. Tjong: Novel nanoparticle-reinforced metal matrix composites with enhanced mechanical properties. *Adv. Eng. Mater.* **9**, 639 (2007).
10. A. Mortensen and J. Llorca: Metal matrix composites. *Annu. Rev. Mater. Res.* **40**, 243 (2010).
11. J.P. Kruth, G. Levy, F. Klocke, and T.H.C. Childs: Consolidation phenomena in laser and powder-bed based layered manufacturing. *CIRP Ann. Manuf. Technol.* **56**, 730 (2007).
12. M. Das, V.K. Balla, D. Basu, S. Bose, and A. Bandyopadhyay: Laser processing of SiC-particle-reinforced coating on titanium. *Scr. Mater.* **63**, 438 (2010).
13. L. Thijs, F. Verhaeghe, T. Craeghs, J.V. Humbeeck, and J.P. Kruth: A study of the microstructural evolution during selective laser melting of Ti-6Al-4V. *Acta Mater.* **58**, 3303 (2010).
14. Y. Zhou and G.H. Wu: *Analysis Methods in Materials Science—X-ray Diffraction and Electron Microscopy in Materials Science*, 2nd ed. (Harbin Institute of Technology Press, Harbin, China, 2007).
15. M. Agarwala, D. Bourell, J. Beaman, H. Marcus, and J. Barlow: Direct selective laser sintering of metals. *Rapid Prototyping J.* **1**, 26 (1995).
16. X.B. Zhou and J.Th.M. De Hosson: Reactive wetting of liquid metals on ceramic substrates. *Acta Mater.* **44**, 421 (1996).
17. Z.F. Yuan, J.J. Ke, and J. Li: *Surface Tension of Metals and Alloys*, 1st ed. (Science Press, Beijing, China, 2006).
18. P.M. Ajayan, L.S. Schadler, and P.V. Braun: *Nanocomposite Science and Technology* (Wiley-VCH Verlag GmbH, Weinheim, 2003).
19. Q.B. Jia and D.D. Gu: Selective laser melting additive manufacturing of Inconel 718 superalloy parts: Densification, microstructure and properties. *J. Alloys Compd.* **585**, 713 (2014).
20. P. Fischer, V. Romano, H.P. Weber, N.P. Karapatis, E. Boillat, and R. Glardon: Sintering of commercially pure titanium powder with a Nd:YAG laser source. *Acta Mater.* **51**, 1651 (2003).
21. T. Vilaro, C. Colin, J.D. Bartout, L. Nazé, and M. Sennour: Microstructural and mechanical approaches of the selective laser melting process applied to a nickel-base superalloy. *Mater. Sci. Eng., A* **534**, 446 (2012).
22. H. Yan, P.L. Zhang, Z.S. Yu, C.G. Li, and R.D. Li: Development and characterization of laser surface cladding (Ti,W)C reinforced Ni-30Cu alloy composite coating on copper. *Opt. Laser Technol.* **44**, 1351 (2012).
23. Z.M. Wang, K. Guan, M. Gao, X.Y. Li, X.F. Chen, and X.Y. Zeng: The microstructure and mechanical properties of deposited-IN718 by selective laser melting. *J. Alloys Compd.* **513**, 518 (2012).
24. V. Erukhimovitch and J. Baram: Crystallization kinetics. *Phys. Rev. B* **50**, 5854 (1994).
25. A. Simchi and H. Pohl: Effects of laser sintering processing parameters on the microstructure and densification of iron powder. *Mater. Sci. Eng., A* **359**,119 (2003).
26. K. Arafune and A. Hirata: Thermal and solutal marangoni convection in Ln-Ga-Sb system. *J. Cryst. Growth* **197**, 811 (1999).
27. R.M. Mahamood, E.T. Akinlabi, M. Shukla, and S. Pityana: Scanning velocity influence on microstructure, microhardness and wear resistance performance of laser deposited Ti_6Al_4V/TiC composite. *Mater. Des.* **50**, 656 (2013).
28. L.Y. Sheng, F. Yang, T.F. Xi, and J.T. Guo: Investigation on microstructure and wear behavior of the NiAl–TiC-Al_2O_3 composite fabricated by self-propagation high-temperature synthesis with extrusion. *J. Alloys Compd.* **554**, 182 (2013).

Supplementary Material

To view supplementary material for this article, please visit http://dx.doi.org/jmr.2014.130.

https://doi.org/10.1557/jmr.2014.130 Published online by Cambridge University Press